Acta Cryst. (1977). A33, 161–168

The Intensity Distribution of X-ray *Pendellösung* Fringes

BY M. WADA* AND N. KATO

Department of Applied Physics, Faculty of Engineering, Nagoya University, Nagoya 464, *Japan*

(*Received* 28 *May* 1976; *accepted* 7 *July* 1976)

The intensity distribution of X-ray diffraction topographs in Laue cases was measured for Si perfect crystals by microdensitometry with an accuracy of 1% at the maximum intensity. Both section and traverse topographs taken with {220} and {440} reflexions were studied, but the section topographs were the main interest. A least-squares analysis shows that the observed intensities can be represented well by the sum of two terms: the dynamical term based on the spherical wave theory and the kinematical term which has a form of attenuation because of the normal absorption. The latter term, however, is very small and its ratio to the former, evaluated at zero depth, was about 10^{-3} in the perfect crystals available.

1. Introduction

The *Pendellösung* phenomenon is one of the fundamental subjects of dynamical diffraction in nearly perfect crystals. For X-rays, the *Pendellösung* fringes of Laue cases were observed by Kato & Lang (1959) and theoretically treated by regarding the incident wave as a spherical wave (Kato, 1960, 1968*a*,*b*). The theoretical predictions were confirmed as far as the geometric aspects of the fringes were concerned (Hattori & Kato, 1966; Homma, Ando & Kato, 1966). Accurate and absolute measurements of the structure factors were successfully performed on the basis of these studies (Tanemura & Kato, 1972; Aldred & Hart, 1973*a*,*b*). The method was also applied to neutrons to determine the scattering amplitude (Shull & Oberteuffer, 1972).

Nevertheless, as the next stage of the investigation it is desirable to examine the extent to which the theory can correctly predict the intensity distribution of the *Pendellösung* fringes. For electrons, it is believed that the simple elastic scattering theory based on the two-beam approximation cannot satisfactorily describe the intensity distribution of the equal-thickness fringes (Uyeda & Nonoyama, 1965; Cowley, 1975). For X-rays, no detailed study has been reported on this subject, except for that of Batterman & Patel (1968). They measured the spatial distribution of the diffracted intensity with a wide incident beam for Ge. Their main interest, however, was the fringe positions for determining the structure factors.

The principal aim of this paper is to examine the spherical wave theory for perfect crystals. For this reason we used Si single crystals which were, as far as possible, perfect and confined our interest mainly to the section topographs in symmetrical Laue cases, which are simplest from the theoretical viewpoint.

In conclusion, the spherical wave theory is reasonably correct. Experimentally, however, it turned out that a small term due to kinematical diffraction has to be introduced to describe the intensity distribution of the topographs. The latter subject, which is connected with X-ray characterization of real crystals, is also dealt with to some extent in this study.

2. Intensity formulae

The results obtained from the dynamical theory are summarized (see, for example, Azaroff, 1974). The following formulae are applicable to absorbing crystals, unpolarized X-rays and any geometric conditions in Laue cases, unless stated otherwise.

Section topographs

The intensity distribution in the reflecting plane due to a spherical wave is given by

$$I_g(x,z) = A|\beta|^2 \exp(-\mu_0 z/\cos\theta_B) \times [|J_0(\beta\zeta)|^2 + |\cos 2\theta_B|^2 |J_0(|\cos 2\theta_B|\beta\zeta)|^2], \quad (1)$$

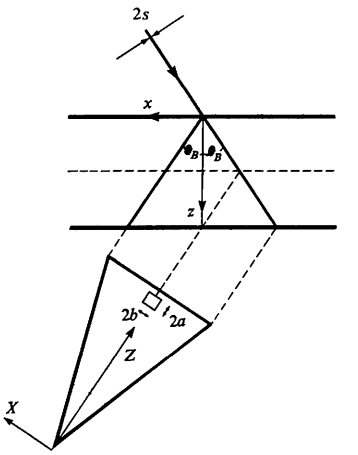

Fig. 1. Section topographs. The coordinate systems and the slits used are shown.

* Present address: The Central Research Laboratory, Fuji Photo Film Co., Asaka, Saitama Prefecture, Japan.

where A is a constant and the argument $\beta\zeta$ of the zero-order Bessel function J_0 is given by

$$\zeta=(z^2\sin^2\theta_B-x^2\cos^2\theta_B)^{1/2} \tag{2}$$

$$\beta=\frac{e^2}{mc^2}\frac{2\lambda}{v}\frac{(F_gF_{-g})^{1/2}}{\sin 2\theta_B}. \tag{3}$$

The other notations used are:

x and z: The coordinates normal and parallel to the net plane, the origin being taken at the entrance point (see Fig. 1).

μ_0: The normal linear absorption coefficient.

θ_B: The Bragg angle.

F_g: The structure factor of the gth order, including the dispersion effects.

λ: The wavelength.

v: The unit-cell volume.

e,m,c: The physical constants in the conventional usage.

When the asymptotic expression of the Bessel function is used for the large argument, equation (1) becomes

$$\begin{aligned}I_g(x,z)&=\frac{A|\beta|}{\pi\zeta}\exp(-\mu_0 z/\cos\theta_B)\\&\times\left[\cos\left(2\beta^r\zeta-\frac{\pi}{2}\right)+|\cos 2\theta_B|\cos\left(2\beta^r|\cos 2\theta_B|\zeta-\frac{\pi}{2}\right)\right.\\&\left.+\cosh(2\beta^i\zeta)+|\cos 2\theta_B|\cosh(2\beta^i|\cos 2\theta_B|\zeta)\right],\end{aligned} \tag{4}$$

where the superscripts r and i denote the real and imaginary parts. This formula can be used for thick crystals.

Traverse topographs

By integrating equation (1) with respect to the x coordinate, one obtains the expression for the traverse topograph for the symmetrical Laue case with respect to the entrance surface. This expression is sufficiently accurate, unless β^i/β^r is greater than 0·1. The variable z can be replaced by the distance t of the observation point from the entrance surface in this particular case. The formula is given by

$$\begin{aligned}R_g(t)&=\frac{\pi}{2}A\exp-(\mu_0 t/\cos\theta_B)\\&\times\{W(2\sin\theta_B\beta^r t)+W(2\sin\theta_B|\cos 2\theta_B|\beta^r t)\\&+[I_0(2\sin\theta_B\beta^i t)-1]\\&+|\cos 2\theta_B|[I_0(2\sin\theta_B|\cos 2\theta_B|\beta^i t)-1]\},\end{aligned} \tag{5}$$

where $W(\xi)$ is the Waller integral defined by

$$W(\xi)=\int_0^{\xi}J_0(\varrho)\mathrm{d}\varrho, \tag{6}$$

and I_0 is the modified Bessel function of the zeroth order.

Equations (1), (4) and (5) are the ideal intensity distributions for an infinitesimal slit. In practice, however, one needs to use a slit of finite size both for taking X-ray topographs and for the densitometry described below. Some convolution procedures, therefore, are required to obtain the intensity curves which can be directly compared with experiment. The details are given in Appendix *A*.

3. Photographic characteristics of nuclear emulsion plates

In the present experiment it is intended to measure the intensity distribution of two-dimensional diffraction patterns with high spatial resolution. For this purpose, the photographic method of measuring X-ray intensity seems most adequate and reliable. Unfortunately, however, the characteristics of nuclear plates and X-ray radiations have not been well studied. Here, we are concerned with (i) the linearity between the photographic darkness (D) and the total energy (E) recorded per unit area, and (ii) the reciprocal relation between the intensity (I) and the exposure time (T). These two points were particularly examined for the combination of the Ag $K\alpha_1$ line and the Ilford L4 plate with an emulsion 100 μm thick.*

The conventional apparatus for traverse topographs was used and the intensity of the incident beam was reduced stepwise by inserting Al sheets in its path. Each sheet has a transmission ratio of $0{\cdot}72\pm0{\cdot}01$ (determined by a counter method). Two diaphragms were put in the path of the Bragg reflected beam to eliminate the scattered rays from the Al sheets and the specimen.

For a wedge-shaped specimen of Si, we obtained the traverse topographs illustrated in Fig. 2. Under the present conditions, it can be assumed that the recorded intensities along each line of the *Pendellösung* fringes are reduced step by step by the transmission ratio of a single Al sheet. The darkness D was measured by means of a standard microdensitometer along a line perpendicular to the fringes. The estimated densitometry error is 0·03 on the absolute scale. Fig. 3 shows a graph of D *vs* I. Here, the intensity I is on an arbitrary scale but with the fixed ratio of 0·72 between the neighbouring plots, and the ordinate is an effective darkness $D_e=D-D_d$, in which D_d is the darkness corresponding to the unexposed part of the photographic plate. The plotting sequence specified by the numerical labels refers to the different exposure times. The results indicate that the linearity between D_e and I holds up to a D_e value of 3·5.

Because all experiments were performed under the same conditions of X-ray source operation, one can assume that the intensity of the incident beam on the

* The photographic procedure was: (*a*) Development in Kodak D19b at 0 °C for 30 min, and at increasing temperature to 8 °C from 0 °C for an additional 30 min. (*b*) Stopping in acetic acid at 8 °C for 30 min. (*c*) Fixing ($NaHSO_3$: 30 g, $Na_2S_2O_3$: 300 g in 1 l solution) for 3 h. (*d*) Rinsing in water for 10 h.

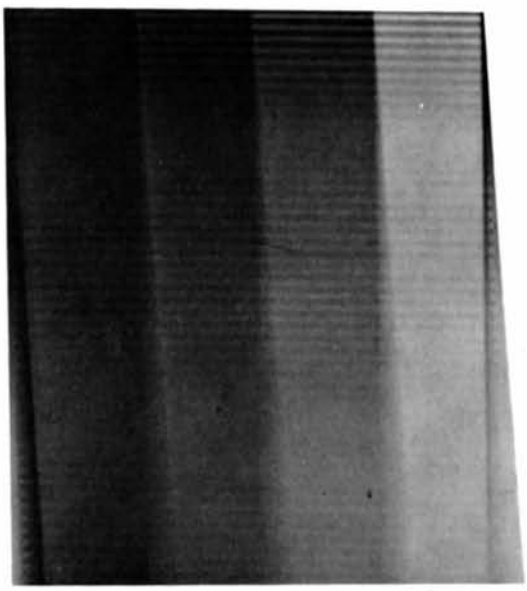

Fig. 2. The traverse topograph used for examining the photographic characteristics of nuclear emulsion plates.

[*To face p.* 162

Al sheets must be identical. Then, $E = I \times T$ is the total energy per unit area. Fig. 4 shows the relation between D_e and E, which was obtained from all the data in Fig. 3. Again, the linearity between E and D_e holds. This implies that the photographic reciprocity is satisfied over the range studied. In the present experiment, the exposure times cover the range 6 to 60 h.

4. Experiments without a monochromator

The two wedge-shaped specimens were prepared from a dislocation-free single crystal of Si. It was grown by the Czochralski method and the pulling direction was [111]. The wedge angles of the specimens were about 12°, and the surfaces were nearly perpendicular to the growth direction. Both section and traverse topographs taken with 220, $\bar{2}\bar{2}0$, 440 and $\bar{4}\bar{4}0$ reflexions were studied. The symmetrical Laue conditions were satisfied within the accuracy of 2°.

The photographic darkness was measured with the same microdensitometer as was used for examining the characteristics of the nuclear plate. In the case of traverse topographs, the darkness distribution was measured along a line perpendicular to the fringes. In the case of section topographs the darkness distribution was measured along the bisector (Z) of the wedge-shaped pattern (see Fig. 1).

As mentioned above, for comparing theory with experiment, one needs to correct the effects of the slit size. The sizes used in practice are listed in Table 1. The corresponding corrections are listed in Table 2. In principle, the effects of the vertical divergence of the X-rays have to be corrected. In the present experimental conditions, however, a single point of the specimen was projected onto the recording plate with a vertical distance less than 5 μm, so that the correction was regarded as negligible.

Table 1. *Slit size* (μm)

(*a*) X-ray topographs (2*s* in Fig. 1)

	Section	Traverse
{220}	35	100
{440}	40	100

(*b*) Densitometry

Slit size	Section	Traverse
2*a*	20	20
2*b*	30	100

Table 2. *The slit-size correction*

Fringe order	Uncorrected	Corrected
6 (max.)	3·00	2·37
(min.)	0·47	1·13
10 (max.)	1·13	1·02
(min.)	0·63	0·72
20 (min.)	0·10	0·15
(max.)	0·56	0·52
25 (min.)	0·07	0·09
(max.)	0·41	0·39
30 (min.)	0·11	0·12
(max.)	0·26	0·26

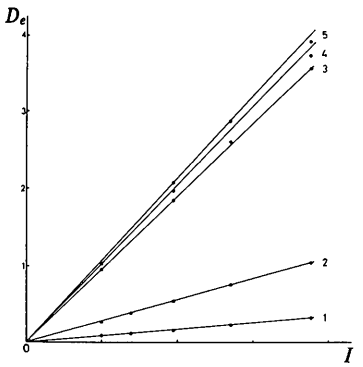

Fig. 3. Linearity between the effective darkness D_e and the X-ray intensity I.

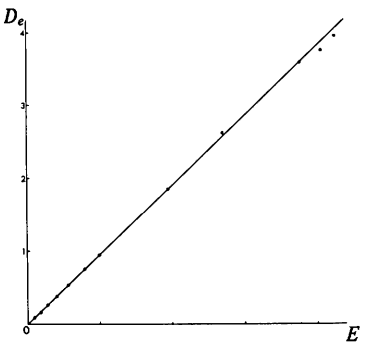

Fig. 4. Reciprocity of E, (intensity) × (exposure time), with respect to the darkness.

Section topographs

The topographs obtained were standard (*e.g.* Figs. 4–31 in Azaroff, 1974). Examples of the darkness curves (D curves) are shown in Fig. 5(*a*) and (*b*). The zero value of the darkness was always set at the darkness level D_d, corresponding to the unexposed part of the nuclear plate (*cf.* § 3). An appreciable background was observed in a region surrounding the topograph. Presumably this is due to fluorescence and Compton scatterings. It was practically homogeneous in the vicinity of the topographs, except at the tip where photographic halation was inevitable. The homogeneous part was about 0·02 for {220} reflexions and 0·08 for {440} reflexions. For this reason, we subtract these constant amounts D_S from the D curves. The corrected darkness values are denoted by D_0.

In Fig. 5 the darkness in the A region exceeds the value $D_0 = 3{\cdot}0$. We deliberately omitted the several fringes in this region to ensure linearity of D *vs* I and avoid the effects of halation. The irregular be-

haviour (fading) of the fringes denoted by arrows is due to X-ray polarization. This has been thoroughly discussed by Hattori, Kuriyama & Kato (1965) and Hart & Lang (1965).

The darkness curves were analysed by least squares. The following observation equations were assumed:

$$\text{Case I} \quad D_0^{(j)} = AD_T^{(j)} \tag{7}$$

$$\text{Case II} \quad D_0^{(j)} = AD_T^{(j)} + B \tag{8}$$

$$\text{Case III} \quad D_0^{(j)} = AD_T^{(j)} + BD_B^{(j)}. \tag{9}$$

Here A and B are adjustable parameters. The superscript (j) indicates the order of the maxima and minima of the D curves. When the extremes were appreciable in the fading region, they were treated in the same way as the extremes in the regular fringe region. D_T is the theoretical value calculated from equation (1) or (4) with the slit-size correction described in Appendix *A*. The numerical values of the structure factors and the normal absorption coefficient μ_0 used in the expressions of I_g are given in Appendix *B*. D_B is a trial function to obtain the best fit in the least-squares analysis.

In case I, the residuals were larger than the densitometric errors of 0·03, and were negative for the maxima of the fringes, and positive for the minima. In case II, the residuals were comparable to 0·03 but there was a systematic tendency that occurs more frequently for the negative residuals in the thicker region. The best fit was obtained by taking

$$D_B = \exp -\mu_0 t/\cos\theta_B \tag{10}$$

in case III. The parameters A and B were $114{\cdot}8 \pm 1{\cdot}2$ and $0{\cdot}13 \pm 0{\cdot}01$ respectively, for example, in the (220) case for specimen I. The r.m.s. of the residuals was 0·026 in this case.

Fig. 6(*a*) and (*b*) illustrates how the observed D curves (full lines) fit the theoretical curves (dotted lines). Here, the horizontal scale is linearly adjusted. The half-dotted lines show the term BD_B in each case. In Table 3 the B/A ratios are listed for the two samples.

Traverse topographs

A similar analysis was performed for the D curves of the traverse topographs. In this case, one can measure the intensity from the first fringe without affecting the D *vs* I linearity or the halation. The best fit is obtained when equation (8) is assumed as the observation equation. Fig. 7 shows the final results corresponding to the section topographs of Fig. 6. The positional shifting of the lower-order fringes is due to the rounding of the wedge-shape so that the discrepancy is trivial as far as the diffracted intensities are concerned. The B/A ratios are also listed in Table 3.

Adopting the observation equation (8) seems inconsistent with adopting equation (10) for D_B in the case of section topographs. Actually, $K\alpha_2$ and general rays may contribute to the background more in the traverse experiments in which the wider beam has to be used. Moreover, one cannot guarantee the homogeneity of the background D_S inside the topographs. For these reasons the arguments for the inconsistency mentioned above are meaningless. The treatment of traverse topographs is to be regarded as a purely phenomenological.

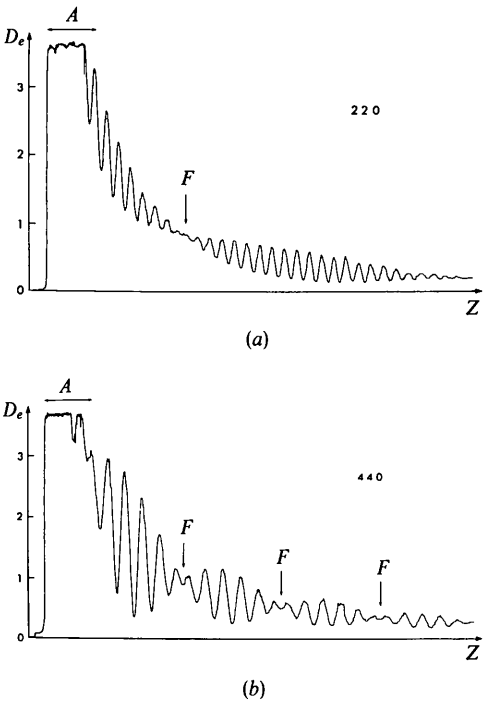

Fig. 5. The observed darkness curves. (*a*) 220 reflexion. (*b*) 440 reflexion.

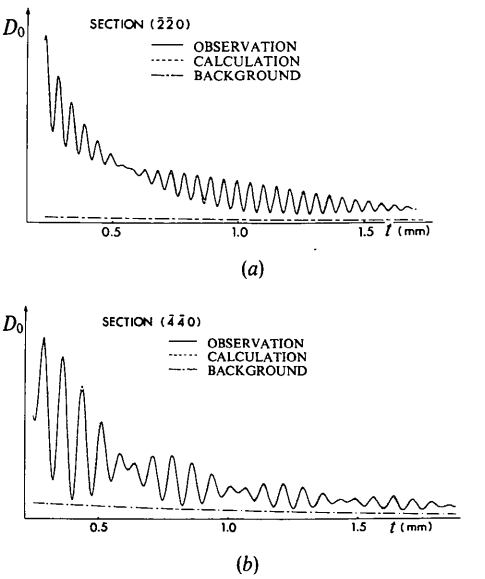

Fig. 6. Section topographs. Comparison between the observed and theoretical darkness curves. (*a*) ($\bar{2}\bar{2}0$) section. (*b*) ($\bar{4}\bar{4}0$) section.

Table 3. *The ratio of B/A*

(*a*) Section topographs

	Sample I		Sample II	
	Without monochromator	With monochromator	Without monochromator	With monochromator
220	$1{\cdot}2\times10^{-3}$	$0{\cdot}7\times10^{-3}$	$0{\cdot}8\times10^{-3}$	$0{\cdot}5\times10^{-3}$
$\bar{2}\bar{2}0$	$0{\cdot}7\times10^{-3}$	$0{\cdot}5\times10^{-3}$	$0{\cdot}8\times10^{-3}$	$0{\cdot}4\times10^{-3}$
440	$2{\cdot}8\times10^{-3}$	$1{\cdot}2\times10^{-3}$	$3{\cdot}4\times10^{-3}$	$1{\cdot}0\times10^{-3}$
$\bar{4}\bar{4}0$	$3{\cdot}9\times10^{-3}$	$1{\cdot}6\times10^{-3}$	$3{\cdot}6\times10^{-3}$	$1{\cdot}5\times10^{-3}$

(*b*) Traverse topographs for sample II, without monochromator

220	0·10	440	0·23
$\bar{2}\bar{2}0$	0·11	$\bar{4}\bar{4}0$	0·16

5. Experiments with a monochromator

The general rays and the $K\alpha_1$ radiation propagating with an off-Bragg condition may contribute to the topographs, especially to the background, even in the case of section topographs. In fact, the angular divergence of the incident beam without a monochromator was nearly one minute of arc, which is narrow enough to separate $K\alpha_1$ and $K\alpha_2$ lines but much larger than the angular range of the Bragg reflexion, *e.g.* $\Delta\theta_B=2{\cdot}1''$ for {220} reflexions. In order to clear up this ambiguity, the same section topograph experiments were repeated with the monochromatized incident beam.

An asymmetric monochromator using the 111 reflexion was made from a Si perfect crystal in order to obtain a beam of narrow width. The reflexion arrangement for the specimen was the (+, +) setting to eliminate the contribution of general rays from the Bragg-reflected intensity of the specimen. The characteristics of the monochromatized beam were as follows: beam width: 12 μm, calculated angular width: 7″. The beam width is sufficiently narrow for our purposes.

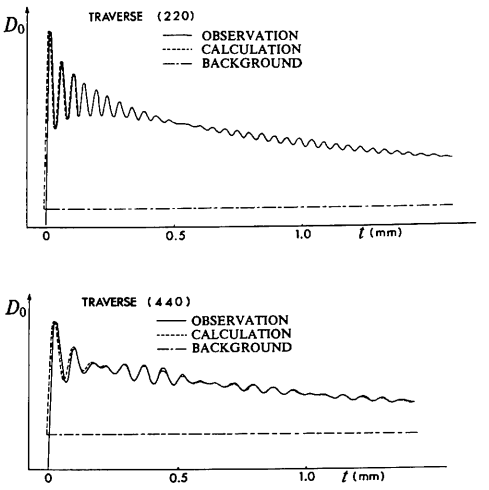

Fig. 7. Traverse topographs. Comparison between the observed and theoretical darkness curves. (*a*) (220) traverse. (*b*) (440) traverse.

The angular width, on the other hand, is enough to cover the angular width $\Delta\theta_B$ of the specimen. Thus, the incident beam still has the character of a spherical wave, as far as we are concerned, with the intensity along the net plane.

The procedures for obtaining D curves and the least-squares analysis were identical to those in § 4.* As to fitting the observed darkness to the theoretical values at the extremes, the results were very similar to those in the experiments without the monochromator. The B/A ratios which are listed in Table 3, however, are slightly decreased. For {220} reflexions the ratios were about one-half of the values in the experiment without the monochromator, and were nearly one third for {440} reflexions.

6. Discussion and conclusions

The Pendellösung fringes

As far as the behaviour of the fringes is concerned, the observed intensity distributions are in agreement with the theoretical predictions from equation (1) or equations (4) and (5) within the experimental error of 0·03 on the D scale, *i.e.* 1% of the maximum intensity on the intensity scale. This implies that the spherical wave theory is satisfactory for understanding *Pendellösung* fringes in Laue cases, regarding not only their geometric character but also the intensity distribution. Also, the prevailing considerations on X-ray polarization in the dynamical theory are adequate within the accuracy of the present experiments. It is worth emphasizing that the intensity distribution of the topographs is more complex than the conventional rocking curves so that the present experiment gives a more critical justification of the dynamical theories for perfect crystals. In this connexion, it is important that the present least-squares method includes only two adjusting parameters, A and B. One can conclude, therefore, that the numerical values of the physical constants listed in Appendix B are reasonably correct.

* The parallel and perpendicular components of X-ray polarization must have the same intensity in the total reflexion range of the monochromator. Unlike experiments on the integrated intensity, therefore, equation (1) has to be used for the present double-crystal experiments.

The background

Experimentally, it is concluded that a background term has to be added to explain completely the intensity distributions of section and traverse topographs. For the reason mentioned at the end of § 4, however, we shall only discuss the section topographs.

The slight but appreciable difference in the ratios of B/A for the experiments with and without the monochromator suggests that the background is due to the off-Bragg waves. This implies that the background originates from the region along the incident beam and diffracts in the direction of the Bragg reflexion in a kinematical sense. In fact, the form of the best fitting function of D_B confirms this interpretation.

It is significant that the change in B/A is rather small in the experiments with and without the monochromator. Although the angular width of the incident beam was reduced to about one tenth by the monochromator, the reduction of B/A is only of the order of one half or one third. This implies that the background arises from the incident beam which nearly satisfies the Bragg condition. General X-rays are definitely irrelevant to the background.

The model of the crystal waves inside the crystal is illustrated in Fig. 8. According to the dynamical theory, that part of the incident waves satisfying the Bragg condition propagates within the Borrmann fan starting from the entrance point E. The remainder, which do not practically satisfy the Bragg condition, propagate along the two edges of the Borrmann fan. The waves propagating in the direction of the incident beam may encounter a distorted region where the waves satisfy the Bragg condition and are diffracted in a kinematical sense. Thus, if one observes the crystal waves at a point P on the exit surface, the wave fields consist of two parts: the dynamical wave and the kinematical wave originating from the region D along the incident beam.

Obviously, one may also imagine the scattered waves of the dynamical wave and the rescattering of the kinematical wave mentioned above. The principle of the Born approximation, however, means that the contributions of such waves at point P must be small unless the lattice distortions are very large. Thus, the above-mentioned model, based on the Born approximation combined with the ray consideration, is reasonable.

Within the scope of the present experiments it is difficult to state conclusively what the physical origin of the background is. Since, however, the magnitude of B/A is larger in the case of {440} reflexions than in the case of {220} reflexions, it is suggested that the background is caused by lattice distortions of the displacement type, such as thermal vibrations or the distortion surrounding a cluster of point defects. In this respect, it is worthwhile referring to the recent work of Patel (1975), in which he observed small humps on both sides of the tails of the rocking curves in Si single crystals, when the specimens were properly heat-treated. Our specimens would be similar to the specimens of his experiment before heat treatment. The topographic experiments are complementary to the rocking-curve experiments.

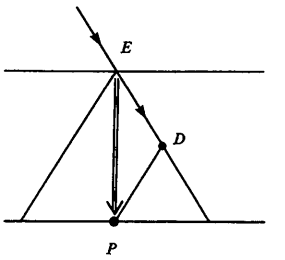

Fig. 8. The model of the wave fields. The double arrow (EP): the dynamical wave. The single arrow (EDP): the kinematical wave.

In conclusion, it has been experimentally confirmed that the diffracted intensity for nearly perfect crystals is well described by the dynamical diffraction term with a smaller kinematical diffraction term. The former is given by equation (1) or (4) for section topographs. The latter has the functional form of equation (10) which is expected from the normal absorption along the kinematical beam paths.

The authors wish to thank Mr Katagawa for his help, for the computer program for the least-squares analysis and for the slit corrections.

APPENDIX *A*

Correction of the slit size

The present considerations are limited to the symmetrical Laue case which has a special geometrical condition that the bisector plane of the wedge crystal is set vertically. Then, the intensity distributions of the diffraction pattern and of the reflexion plane inside the crystal must be mutually proportional, provided that the coordinates (X,Z) of the diffraction pattern and (x,z) of the reflexion plane are connected by the linear transformation:

$$X = x\cos\theta_B, \quad Z = \tfrac{1}{2}z\cot W/2. \qquad (A1a,b)$$

Here, θ_B is the Bragg angle and W the wedge angle of the crystal. The coordinate systems and the slit configurations are illustrated in Fig. 1.

First we shall consider the correction due to the slit placed in front of the specimen while taking topographs. Let $I_g(x,z)$ be the intensity distribution in the reflexion plane [given by either equations (1) or (2)], and $J_g(X,Z)$ be the intensity distribution of the diffraction pattern taken with a vertical slit of width $2s$. Then, the relation between J_g and I_g is

$$J_g(X,Z) = (1/2s)\int_{-s}^{s} I_g[c_1(X-u), c_2 Z]\,\mathrm{d}u, \qquad (A2)$$

where c_1 and c_2 represent $\sec\theta_B$ and $2\tan W/2$ respectively.

Next, we shall consider the correction due to the rectangular slit employed in the densitometry, its size being $2a$ and $2b$ in the directions of Z and X respectively. Assuming that the photographic darkness is proportional to the averaged intensity taken over the slit area, one obtains the theoretical darkness D_T, which has to be compared with D_0 mentioned in the text, in the form

$$D_T(X,Z) = K\int_{-a}^{a} dw \int_{-b}^{b} dv \int_{-s}^{s} I_g[c_1(X+v-u), c_2(Z+w)]du. \quad (A3)$$

Here, the proportional factor includes the factors $1/2a$, $1/2b$ and $1/2s$.

The first integral with respect to w is evaluated approximately by the use of Simpson's formula (Jeffreys & Jeffreys, 1959)

$$L(x,Z) \equiv \int_{-a}^{a} I_g[x, c_2(Z+w)]dw \quad (A4a)$$

$$\simeq \frac{a}{3}\{I_g[x,c_2(Z+a)] + 4I_g(x,c_2Z) + I_g[x,c_2(Z-a)]\}. \quad (A4b)$$

This approximation is justified because the variation of I_g along z is relatively smooth. The remaining double integral can be reduced to a single integral by the use of the transformation

$$p = v-u, \quad q = v+u \quad (A5a,b)$$

In fact, inserting the relation $(A4a)$ into equation $(A3)$:

$$D_T(X,Z) = K\int\int L[c_1(X+p), Z]\left|\frac{\partial(u,v)}{\partial(p,q)}\right| dpdq, \quad (A6)$$

where the integral domain is the rectangle composed of the domains A, B and C illustrated in Fig. 9, and $\partial(u,v)/\partial(p,q)$ is the Jacobian of the transformation $(A5)$, which is equal to $1/2$. The integration of q can be performed irrespective of the functional form of L. When s is larger than or equal to b:*

* In the reverse case, the roles of b and s have to be interchanged in equation $(A7)$.

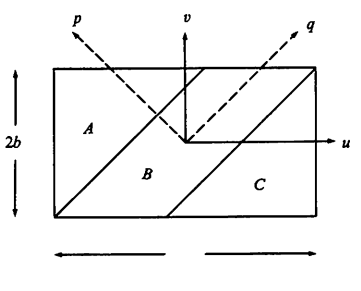

Fig. 9. The coordinate transformation for the slit-size correction.

$$D_T(X,Z) = K\int_{s-b}^{s+b} L[c_1(X+p)Z]\,[(b+s)-p]dp + 2bK\int_{b-s}^{s-b} L[c_1(X+p),Z]dp + K\int_{-(b+s)}^{b-s} L[c_1(X+p),Z]\,[(b+s)+p]dp. \quad (A7)$$

Each term corresponds to the integrals in the domains A, B and C respectively. The integration was again performed numerically with Simpson's method. For our purpose, $D_T(O,Z)$ is significant.

In the case of traverse topographs the function I_g, and consequently L, is independent of x. Therefore, the theoretical darkness curve is simply given by

$$D_T(X,Z) = (4bs)KL(Z),$$

where $L(Z)$ is the same as the expression $(A4b)$ but the variable x can be suppressed.

In Table 2, the corrected and uncorrected values of the theoretical darkness of (220) section topographs are compared. Up to the fringes of the 24th order, the amounts of the correction exceed the error in the densitometry. The correction, therefore, is very significant in the present experiment.

APPENDIX *B*

The structure factors and the linear absorption coefficient

Since Si has a centre of symmetry, one can write

$$(F_gF_{-g})^{1/2} = F_g^r + iF_g^i,$$

neglecting the higher terms, where the suffixes r and i indicate the real and imaginary parts. For the real part, the following experimental values were adopted (Tanemura & Kato, 1972): $F_g^r(220) = 67{\cdot}7$, $F_g^r(440) = 43{\cdot}2$.

The imaginary part F_g^i is composed of three terms in the form

$$F_g^i = F_g^i(\mathrm{PH}) + F_g^i(\mathrm{CO}) + F_g^i(\mathrm{TDS}),$$

where PH, CO and TDS are the abbreviations for photoelectric effect, Compton scattering and thermal diffuse scattering. In the present experiments, the theoretical values adopted are given in Table 4. For F_g^i(PH), the dipole, dipole–octupole and quadrupole terms are taken into account. The evaluation of F_{440}^i(TDS) was not easy so that the value of F_{220}^i was tentatively used. In fact, no significant difference was noticed in the value of D_T even when F_{440}^i(TDS) was neglected.

For the normal absorption coefficient, the following experimental value of Hildebrandt, Stephenson & Wagenfeld (1973) was used: $\mu_0 = 7{\cdot}32\ \mathrm{cm}^{-1}$.

Table 4. *Theoretical values adopted for* F_g^i

$F^i_{220}(\mathrm{PH})^{(a)}$	=0·340 (⊥ polarization)
	=0·339 (∥ polarization)
$F^i_{440}(\mathrm{PH})^{(a)}$	=0·309 (⊥ polarization)
	=0·302 (∥ polarization)
$F^i_{220}(\mathrm{CO})^{(b,c)}$	=0·009
$F^i_{440}(\mathrm{CO})^{(b,c)}$	=0·004
$F^i_{220}(\mathrm{TDS})^{(b,c)}$	=0·007
$F^i_{440}(\mathrm{TDS})^{(d)}$	=0·007

(*a*) Hildebrandt, Stephenson & Wagenfeld (1975). (*b*) Sano, Ohtaka & Ohtsuki (1969). (*c*) Giardina & Merlini (1973). (*d*) Tentatively assumed.

References

ALDRED, P. J. E. & HART, M. (1973*a*). *Proc. Roy. Soc.* A**332**, 223–238.

ALDRED, P. J. E. & HART, M. (1973*b*). *Proc. Roy. Soc.* A**332**, 239–254.

AZAROFF, L. V. (1974). *X-ray Diffraction*. New York: McGraw–Hill.

BATTERMAN, B. W. & PATEL, J. R. (1968). *J. Appl. Phys.* **39**, 1882–1887.

COWLEY, J. M. (1975). *Diffraction Physics*, Chap. 9, p. 190. Amsterdam: North-Holland.

GIARDINA, M. D. & MERLINI, A. (1973). *Z. Naturforsch.* **28a**, 1360–1365.

HART, M. & LANG, A. R. (1965). *Acta Cryst.* **19**, 73–77.

HATTORI, H. & KATO, N. (1966). *J. Phys. Soc. Japan*, **21**, 1772–1 .

HATTORI, H., KURIYAMA, H. & KATO, N. (1965). *J. Phys. Soc. Japan*, **20**, 1047–1050.

HILDEBRANDT, G., STEPHENSON, J. D. & WAGENFELD, H. (1973). *Z. Naturforsch.* **28a**, 588–600.

HILDEBRANDT, G., STEPHENSON, J. D. & WAGENFELD, H. (1975). *Z. Naturforsch.* **30a**, 697–707.

HOMMA, S., ANDO, Y. & KATO, N. (1966). *J. Phys. Soc. Japan*, **21**, 1160–1165.

JEFFREYS, H. & JEFFREYS, B. (1959). *Methods of Mathematical Physics*, p. 287. Cambridge Univ. Press.

KATO, N. (1960). *Z. Naturforsch.* **15a**, 369–370.

KATO, N. (1968*a*). *J. Appl. Phys.* **39**, 2225–2230.

KATO, N. (1968*b*). *J. Appl. Phys.* **39**, 2231–2237.

KATO, N. & LANG, A. R. (1959). *Acta Cryst.* **12**, 787–794.

PATEL, J. R. (1975). *J. Appl. Cryst.* **8**, 186–191.

SANO, H., OHTAKA, K. & OHTSUKI, Y. H. (1969). *J. Phys. Soc. Japan*, **27**, 1254–1261.

SHULL, C. G. & OBERTEUFFER, J. A. (1972). *Phys. Rev. Lett.* **25**, 871–874.

TANEMURA, S. & KATO, N. (1972). *Acta Cryst.* A**28**, 69–80.

UYEDA, R. & NONOYAMA, M. (1965). *Jap. J. Appl. Phys.* **4**, 498–512.

Acta Cryst. (1977). A**33**, 168–171

Orientations and Twinning in the Structural Transformation Aragonite-type to Calcite-like in Potassium Nitrate Crystals

BY S. W. KENNEDY AND M. ODLYHA*

Department of Physical and Inorganic Chemistry, The University of Adelaide, Adelaide, SA 5001, *Australia*

(*Received* 7 *June* 1976; *accepted* 11 *August* 1976)

The structural transformation KNO_3 II $\xrightarrow{128\,^\circ C}$ I was studied by X-ray diffraction and microscopy. Orientations measured by diffraction were (*a*) $[10\bar{1}]_I \| [010]_{II}$, $(110)_I \| (001)_{II}$ and (*b*) $[01\bar{1}]_I \| [010]_{II}$, $(11\bar{1})_I \| (100)_{II}$ (rhombohedral indices, $Z=4$ for I). Two orientations measured by optical and surface analysis agree with two previously found for $CaCO_3$ in glaucophane schists. Transformed specimens recrystallized at 180 °C. There is some optical evidence for twinning. The symmetry options of relation (*b*) would allow $(110)_I$ transformation twinning which could simulate mechanical twinning. The possibility of crystallographically controlled mechanisms is discussed.

The transformation of the aragonite to the calcite structure is of interest both for its possible combination of reconstructive and shear-like components in the mechanism of this change of first coordination, and as an indicator in low-grade metamorphism in rocks. This structure change is well known in calcium carbonate: a very similar transformation occurs in potassium nitrate, KNO_3. Below 128 °C potassium nitrate has a closely pseudo-hexagonal aragonite structure (II), space group *Pmcn*, $Z=4$ (Edwards, 1931; Nimmo & Lucas, 1973), and at higher temperatures the high-$NaNO_3$ structure (I), space group $R\bar{3}m$, in which there is considerable thermal oscillation of the NO_3^- ions (Shinnaka, 1962; Strømme, 1969). Though this differs from calcite in the relative mean orientations of the anions the difference must become less significant at higher temperatures because of the increased amplitude of oscillation of the CO_3^{2-} ions. The morphological subcell of calcite is a true cell of KNO_3 I, which grows with similar rhombohedral morphology (Kennedy, 1972). This cell has $Z=4$, $a=7{\cdot}04$ Å, $\alpha=100{\cdot}8^\circ$. The volume change in KNO_3 is 0·7%.

In the aragonite structure the cations are arranged

* Present address: South Australian Institute of Technology, Pooraka, SA 5098, Australia.